Nanoscale

PAPER

View Article Online
View Journal | View Issue

Cite this: *Nanoscale*, 2025, **17**, 15706

Microwave-assisted synthesis of ZnO/$BiNbO_4$ heterojunctions for enhanced hydrogen production†

Maria Kuznetsova, [a] Priscila Hasse Palharim,[b] Caroline Helena Claudino,[b] José Javier Sáez Acuña,[b] Karina P. M. Frin, [b] Christophe Colbeau-Justin,[c] Hynd Remita[c] and Juliana dos Santos de Souza *[b]

Received 22nd April 2025,
Accepted 10th June 2025

DOI: 10.1039/d5nr01637a

rsc.li/nanoscale

This work introduces a novel heterojunction between ZnO and $BiNbO_4$, prepared through a microwave-assisted technique that significantly reduces time and energy consumption for the synthesis. The used method requires 48 minutes to obtain vertically aligned wurtzite ZnO films and 30 minutes to obtain globular orthorhombic/triclinic $BiNbO_4$. The heterojunction exploits the suitable band alignment of ZnO and $BiNbO_4$ to construct an S-scheme structure, achieving enhanced charge separation and transfer. The prepared ZnO/$BiNbO_4$ heterojunction was used as a photoanode for water photosplitting, exhibiting a fourfold increase in photocurrents for oxygen evolution compared to pristine ZnO. The heterojunction has also demonstrated photocatalytic activity for hydrogen production that is 3.5 and 2 times higher than that of bare ZnO and $BiNbO_4$, respectively. These findings highlight the promising potential of ZnO/$BiNbO_4$ heterojunctions for advanced photocatalytic and photoelectrocatalytic applications, particularly in hydrogen production.

Introduction

Bismuth niobate represents a functional class of materials that exhibits chemical and electrochemical stability and photoelectronic activity. These properties can be explored in various applications, including photocatalysis.[1–14] The niobate structure is composed of distorted [NbO_6] octahedra, which exhibit a relatively high energy level of Nb 4d that composes the conduction band (CB). The presence of Bi^{3+} lone pair electrons in the structure promotes a narrowing of the band gap due to the contribution of the Bi 6s orbital to the valence band.[1,2] Bismuth niobate has been successfully used for the photodegradation of organic pollutants or water photosplitting under UV or visible light (Table 1).

$BiNbO_4$ exists in two polymorphs: low-temperature orthorhombic and high-temperature triclinic phases. According to the literature, the orthorhombic α phase is the most suitable from a photocatalytic perspective.[15] The orthorhombic phase is typically obtained at 900 °C, and its irreversible transition to the triclinic phase occurs at 1020 °C.[15,16] Compared to other reported bismuth niobates (see Table 1), orthorhombic $BiNbO_4$ exhibits high band gap (BG) energy and fast recombination rates.[17]

The analysis of Table 1 shows that the photoactivity of bismuth niobates can be improved through nitrogen-doping,[4] adding co-catalysts such as Ag^0,[5] Pt^0 and Bi^0 nanoparticles,[2,11] or by forming heterojunctions with BiOI,[18] BiOCl,[7,8] TiO_2,[8] graphene,[9] C_3N_4,[10] WO_3,[13] AgO or Ag_2O.[14] However, despite all its potential, few modifications have been reported specifically for $BiNbO_4$.[2,12–14]

Recently, our group has shown that a heterojunction formed between $BiNbO_4$ and WO_3 has the potential to be applied as a photoanode for the oxygen evolution reaction driven by simulated sunlight.[13] However, the $BiNbO_4/WO_3$ suffers from a high onset potential, which limits its application in photocatalytic water splitting.

In this sense, coupling $BiNbO_4$ with ZnO represents an advantage, since ZnO shows high photocurrents for oxygen evolution at low potentials.[19–22] ZnO has a high bandgap energy (~3.2 eV),[19] and is well established as a host material for preparing heterojunctions for photoelectrochemical water splitting.[19,23] The coupling of ZnO with another semiconductor reduces its photocorrosion and enhances charge transfer.[19–26]

In this work, we report a novel ZnO/$BiNbO_4$ heterojunction synthesized *via* a microwave-assisted method, which enabled

[a]*Centro de Lasers e Aplicações, IPEN-CNEN/SP, Av. Prof. Lineu Prestes 2242, zip code 05508-000, São Paulo, Brazil*
[b]*Centro de Ciências Naturais e Humanas, Universidade Federal do ABC, 09210-580 Santo André, SP, Brazil. E-mail: juliana.souza@ufabc.edu.br*
[c]*Université Paris-Saclay, UMR 8000 CNRS, Institut de Chimie Physique, Orsay, 91405, France*

†Electronic supplementary information (ESI) available: EDS mapping, XPS survey spectra, electrochemical data and hydrogen generation kinetics. See DOI: https://doi.org/10.1039/d5nr01637a

energy- and time-efficient preparation. The material was thoroughly characterized to elucidate its structural, optical, and photocatalytic properties, as well as the underlying mechanism.

Experimental

Materials

Niobium(v) chloride ($NbCl_5$), bismuth(III) nitrate pentahydrate ($Bi(NO_3)_3{\cdot}5H_2O$), fluorine-doped tin oxide coated glass slide (FTO glass, surface resistivity ~7 Ω sq^{-1}), hexamethylenetetramine (HMT), zinc acetate dihydrate ($(CH_3COO)_2Zn{\cdot}2H_2O$, ZnAc), sodium sulfate (Na_2SO_4), and triethanolamine (TEOA) were purchased from Sigma Aldrich. Ammonium hydroxide solution (NH_4OH) and isopropanol were purchased from LabSynth. AEROXIDE supplied TiO_2 anatase P25.

Synthesis of $BiNbO_4$

10 mL of 0.01 M aqueous $Bi(NO_3)_3{\cdot}5H_2O$ solution was prepared and stirred for 20 min. Separately, 10 mL of 0.01 M aqueous $NbCl_5$ was stirred for 20 min at 70 °C. The $NbCl_5$ solution was then dripped into the $Bi(NO_3)_3{\cdot}5H_2O$ solution, and the resulting mixture was stirred for 30 min. The pH was adjusted to 7.0 using aqueous NH_4OH, followed by an additional 15 min of stirring. Next, 20 mL of the reaction mixture was transferred to a 30 mL borosilicate vial and sealed with a septum that withstands 300 psi of pressure. The system was placed in the cavity of the Monowave 400 microwave (Anton-Paar), operating in monomode. The reaction was carried out in constant-temperature mode at 200 °C for 30 min, using a maximum irradiation power of 750 W. The resulting solid was collected by centrifugation and washed with water and ethanol. The obtained materials were dried in an oven at 60 °C for 24 h and then calcined at 700 °C for 3 h.

Synthesis of ZnO films

First, FTO substrates (1 cm × 2.5 cm) were cleaned by sequentially dipping them in acetone, distilled water, and ethanol, followed by sonication in each solvent for 30 min. The growth of ZnO nanorods directly on the FTO substrate was carried out in 2 stages.

In the first stage, a ZnO seed layer is formed. Aqueous solutions of 0.5 M HMT and 0.5 M ZnAc were prepared. The FTO films were placed on a WS-650MZ-23NPPB spin coater. Then, 125 μL of each solution was dripped onto the FTO substrate and allowed to stand for 5 min. Each film was spin-coated at 600 RPM (revolutions per minute) for 6 seconds and at 3000 RPM for 30 seconds. Finally, the films were calcined at 200 °C for 15 min using a heating ramp of 10 °C min^{-1} in an EDG 3000 muffle furnace.

In the second stage, the ZnO nanorods were grown hydrothermally. Aqueous solutions of 0.1 M HMT and 0.1 M ZnAc were prepared, and 3.5 mL of each solution was transferred to a borosilicate vial containing the FTO substrates with the deposited ZnO nanorods seed layer. A Teflon tape was applied on the surface of the FTO glass with no seed deposition to prevent ZnO growth on that surface. The system was sealed to control the pressure and placed into the cavity of a Discover microwave (CEM), operating in monomode. The microwave synthesis was carried out at 300 W of irradiation power for 48 min, maintaining a constant temperature of 100 °C throughout the process.

After the synthesis, the films were washed with distilled water to remove residual byproducts, then dried at room temperature and atmospheric pressure for 24 h.

Deposition of $BiNbO_4$ onto ZnO films

To prepare the $BiNbO_4$/ZnO electrodes, a suspension of $BiNbO_4$ nanoparticles at a 1 mg mL^{-1} in isopropanol was prepared by sonication for 3 h. Then, 20 μL of the resulting suspension was drop-casted as three layers onto the surface of the ZnO film, allowing each layer to air-dry before applying the next. The resulting material was annealed at 100 °C for 1 h to evaluate the effect of thermal treatment on its activity. The heterojunctions were subsequently named $BiNbO_4$/ZnO and $BiNbO_4/ZnO_T$, where the letter "T" refers to the thermally treated sample.

For comparison, $BiNbO_4$ films were prepared by dripping 20 μL of the same suspension in three layers onto the surface of the FTO substrate, allowing each layer to air-dry before the next was applied.

Characterization

XRD patterns were collected using a Bruker D8 Discover theta–theta diffractometer equipped with a Cu X-ray tube operated at 40 kV and 40 mA. Grazing incidence measurements were performed using a parallel beam optics configuration, which include a Göbel mirror and a 0.2° divergence vertical Soller slit

Juliana dos Santos de Souza

Bachelor's degree in Chemistry from Universidade Estadual Paulista – UNESP, Brazil. Master's and Ph.D. in Chemical Science and Technology from the Federal University of ABC, Brazil. Postdoctoral Fellowship in Fundamental Chemistry at the Laboratory of Molecular Spectroscopy of the Institute of Chemistry, University of São Paulo, Brazil. Dr Juliana Souza is currently an Assistant Professor at the Federal University of ABC. Research interests are focused on Inorganic Chemistry, specifically the synthesis of semiconducting metal oxide nanostructures using microwave-assisted methodologies, the development of multi-hierarchical systems, heterogeneous catalysis, photocatalysis, photoelectrocatalysis, and the creation of devices for energy conversion.

Table 1 A bibliographic survey of bismuth niobates used in photocatalytic and photoelectrocatalytic processes, highlighting synthesis methods, properties and efficiency

Material	Modification	Method of synthesis	Crystalline structure	Morphology modified (non-modified)	Band gap (eV) modified (non-modified)	Application	Light irradiation	Efficiency modified (non-modified)	Ref.
Bi_3NbO_7	Not modified	Hydrothermal 140 °C for 12 h	Cubic	Polyhedral <50 nm	2.72	Phenol photodegradation/ photocatalytic H_2 production	500 W Xe 420 nm cut-off filter	100% after 1 h/ 110 μmol h^{-1} (g cat)$^{-1}$	1
Bi_3NbO_7	Not modified	Hydrothermal 200 °C for 16 h	Cubic	Nanoplates	2.89	Removal of NO in air	300 W tungsten halogen lamp 420 nm cut-off filter	42% after 40 min	3
Bi_3NbO_7	N-doping	Hydrothermal 140 °C for 12 h	Cubic	Nanoflowers (nanoparticles)	2.47 (2.64)	Methylene blue photodegradation	300 W Xe lamp 420 nm cut-off filter	99% (37%) after 2 h	4
Bi_3NbO_7	Ag-loading	Coprecipitation	Cubic	Nanoflakes (flaky shape)	2.43 (2.57)	Methyl orange photodegradation	500 W Xe lamp (400–800 nm)	94% (50%) after 4 h	5
Bi_3NbO_7	Not modified	Coprecipitation	Cubic	Nearly round nanoparticle	2.75	Rhodamine B photodegradation	500 W Xe lamp 420 nm cut-off filter	95% after 1 h	6
Bi_3NbO_7	Heterojunction with BiOI	Hydrothermal synthesis for 12 h, temperature not informed	Cubic	Globular micrometric (no provided)	1.92 (not provided)	Rhodamine B photodegradation	300 W Xe lamp	60% after 150 min (not measured)	18
$Bi_5Nb_3O_{15}$	Supported on graphene sheets	Hydrothermal 220 °C for 24 h	Orthorhombic	Nanoparticles (same)	2.59 (2.73)	Rhodamine B photodegradation	35 W LED lamp 420 nm cut-off filter	87% (45%) after 80 min	9
$Bi_5Nb_3O_{15}$	C_3N_4	Hydrothermal 200 °C for 24 h	Orthorhombic	Octahedron-like nanoparticles (same)	2.79 (2.90)	4-Chlorophenol (4-CP) and methyl orange (MO) photodegradation	300 W Xe lamp (400–680 nm)	100% (38%) – 4-CP; 94% (28%) – MO	10
$Bi_5Nb_3O_{15}$	Bi^0	Hydrothermal 200 °C for 24 h	Orthorhombic	Nanoplate (same)	2.90 (3.02)	2,4-Dichlorophenoxyacetic acid	300 W Xe lamp 400 nm cut-off filter	87% (15%) after 2 h	11
$BiNbO_4$	Pt^0	Solid state 900 °C/20 h	Orthorhombic	1–3 μm rounded aggregates (same)	~2.8 (same)	Photocatalytic H_2 production	450 W Hg lamp	1320 μmol h^{-1} (400 μmol h^{-1})	2
$BiNbO_4$	Not modified	Layer-by-layer dried at 150 °C and annealing at 550 °C	Orthorhombic	Nanosheet	2.60	Photoelectrochemical oxygen evolution reaction	150 W Xe lamp calibrated to produce 1 sun illumination	0.35 mA cm^{-2} at 0.6 V RHE 1 M NaOH	12
$BiNbO_4$	Heterojunction with WO_3	Microwave-assisted hydrothermal synthesis at 200 °C (750 W) for 30 min and annealing at 700 °C	A mixture of triclinic and orthorhombic	Globular-like (same)	3.2 (not provided)	Photoelectrochemical oxygen evolution reaction	AM 1.5G	0.26 mA cm^{-2} at 0.6 V RHE (not measured)	13
$BiNbO_4$	Heterojunction with AgO or Ag_2O	Microwave-assisted hydrothermal synthesis at 150 °C (550 W) for 30 min and annealing at 700 °C	Orthorhombic	Globular-like (same)	2.17 (3.2)	Rhodamine B photodegradation	AM 1.5G	34% after 1 h (not measured)	14
$BiNbO_4$	Heterojunction with ZnO	Microwave-assisted hydrothermal synthesis at 200 °C (750 W) for 30 min and annealing at 700 °C	A mixture of triclinic and orthorhombic	Globular-like	(3.2)	Photoelectrochemical oxygen evolution reaction/ photocatalytic H_2 production	AM 1.5G	0.19 mA cm^{-2} at 0.6 V RHE (not measured)/ 5.01 mmol g^{-1} h^{-1} (2.34 mmol g^{-1} h^{-1})	This work

on the incident beam, along with a 0.1° divergence parallel plate horizontal slit and a 0.2° vertical Soller slit on the diffracted beam side. The angle of incidence of the X-ray beam was fixed at 0.5°. Data were acquired over a 2θ range of 10° to 60°, with a step size of 0.1° and an acquisition time of 30 s per step. For the SEM analysis, the sample powders were suspended in isopropanol, dropped onto a silicon wafer, and mounted on stubs using conductive carbon tape. The images were acquired using an Inspect F50 scanning electron microscope (Thermo Fisher Scientific). For the HRTEM analyses, suspensions of the materials were prepared by scraping a portion of the sample from the film surface and mixing it with 10 μL of water. The suspension was then drop-cast onto copper grids and dried at room temperature for two days. The images were collected using a transmission electron microscope, the Talos F200X G2 (Thermo Fisher), operated at an accelerating voltage of 200 kV with a field-emission gun. Kelvin probe force microscopy (KPFM) measurements were performed using an NX-10 Park Systems microscope equipped with a NanoSensors Pt/Ir-coated silicon probe (model PPP-EFM), featuring a nominal force constant of 2.8 N m^{-1} and a nominal resonance frequency of 75 kHz. The image size was 2.0 μm × 2.0 μm at a resolution of 256 × 256 pixels, with a frame rate of 0.2 Hz. Image processing was performed using the Gwyddion software. X-ray photoelectron spectroscopy was conducted using a K-alpha XPS (Thermo Fisher Scientific) to quantify the elemental composition and oxidation states of the samples. The analysis employed Al Kα emission, with a vacuum level below 10^{-8} mbar, and charge compensation during the measurements. The spectra were acquired using energies of 200 and 50 eV, with resolutions of 1.0 and 0.1 eV, respectively. The spot size of the incident radiation was 400 μm in diameter, and each spectrum was averaged 20 scans to ensure high statistical accuracy. Ultraviolet photoelectron spectroscopy (UPS) measurements were performed using a Specs XPS/UPS system equipped with a Phoibos 150 analyzer and a CMOS 2D detector. A He I excitation line (21.22 eV) from a UHV gas discharge lamp was used, and a −4 V bias was applied to the samples. The optical properties of ZnO, $BiNbO_4$, $BiNbO_4$/ZnO, and $BiNbO_4/ZnO_T$ films were analyzed by UV-Vis diffuse reflectance spectroscopy (DRS) with an UV–vis–NIR spectrophotometer Cary 5000 Series (Agilent Technologies), with measurements recorded in the 200–800 nm wavelength range.

The photogenerated charge-carrier dynamics in ZnO, $BiNbO_4$, $BiNbO_4$/ZnO, and $BiNbO_4/ZnO_T$ films after UV illumination were studied by the Time-Resolved Microwave Conductivity method (TRMC). A pulsed and tunable laser source (200–2000 nm), equipped with an optical parametric oscillator (EKSPLA, NT342B), was used to excite the samples, while a 30 GHz Gunn diode generated the microwaves. The light energy density incident on the sample was 1 mJ cm^{-2} at 360 nm. TRMC signals were obtained by illuminating the front side of the films and averaging over 200 laser pulses to minimize noise. Reproducibility was assessed by generating TRMC signals from two independent samples of each material.

The principles of TRMC have been described in detail elsewhere.[27,28] The technique measures the relative change in microwave powder reflected from a semiconductor, $(\Delta P(t))/P$, during its excitation by a laser pulse. This change can be related to a small perturbation of the sample's conductivity, as shown in eqn (1).

$$(\Delta P(t))/P = A\Delta\sigma(t) \quad (1)$$

where A is a time-independent proportionality factor. The signal obtained by this technique represents the evolution of the sample's conductivity, $I(t)$, also known as photoconductivity, as a function of time (ns). The primary data extracted from TRMC is the maximum signal intensity (I_{max}), which reflects the number of excess charge carriers generated by the laser pulse. The subsequent decay in the signal is attributed to the reduction in excess (free) electrons.

Photoluminescence (PL) data were obtained in a Cary Eclipse spectrofluorometer (Varian). The films were positioned at a 45° angle relative to the excitation beam in the cuvette sample holder, identical slit conditions were maintained throughout the measurements. Fluorescence lifetime decay was obtained through time-resolved fluorescence (TRF) measurements performed using a FluoTime 300 (PicoQuant GmbH) photocounting setup, equipped with a 375 nm pulsed laser diode (LDH-P-375B) controlled by a PDL 820 drive connected to a computer. The signals were detected at the maximum emission wavelength (424 nm) using an MCP PMT (PicoQuant) photomultiplier. Measurements were conducted with two sets of deposited films, and the reported curves represent the average of 50 000 decay points.

Photoelectrochemical experiments

Electrochemical experiments were performed using a three-electrode system in a cell with a quartz window. ZnO, $BiNbO_4$, $BiNbO_4$/ZnO, and $BiNbO_4/ZnO_T$ films were used as working electrodes, Ag/AgCl (KCl 3 M) was used as a reference, and Pt wire was used as a counter electrode. An aqueous solution of 0.01 M Na_2SO_4 was used as the electrolyte for evaluating the oxygen evolution reaction. Mott–Schottky plots were obtained with an AC amplitude of 10 mV and frequencies of 10, 100, and 1000 Hz in the dark. For the chopped-light linear sweep voltammetry and chronoamperometry measurements the system was positioned at a fixed distance from a solar simulator equipped with a filter suitable for simulating sunlight with an A.M. 1.5 G spectrum and an intensity of 100 mW cm^{-2}, measured with a Newport model 842-PE power meter coupled to an 818-P-001-12 light intensity detector.

Hydrogen generation

The hydrogen generation experiments were conducted in a closed quartz cell (37 mL). For each experiment, ZnO, $BiNbO_4$, $BiNbO_4$/ZnO, and $BiNbO_4/ZnO_T$ films were placed in 20 mL of an aqueous solution containing 25% of TEOA as a hole scavenger. The cell was degassed with Ar for 20 min to remove dissolved oxygen. A helios photoreactor equipped with a medium-

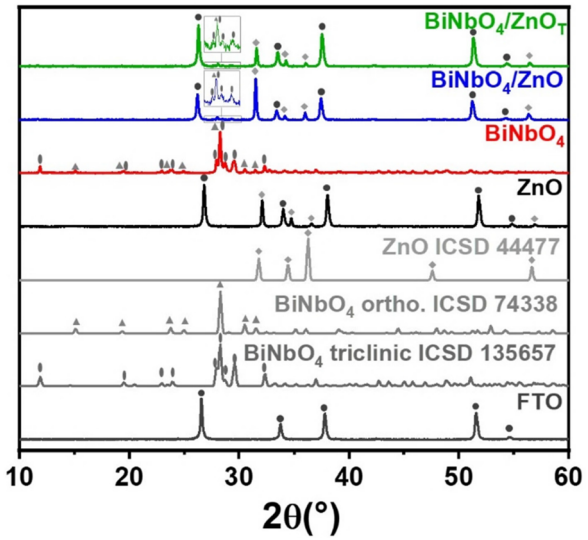

Fig. 1 XRD diffractograms of samples ZnO, $BiNbO_4$, $BiNbO_4$/ZnO and $BiNbO_4/ZnO_T$. For comparison, the XRD of FTO substrate, ZnO ICSD 44477, orthorhombic $BiNbO_4$ ICSD 74338 and triclinic $BiNbO_4$ ICSD 135657 are shown.

pressure UV Hg lamp‡ was the light source. A gas chromatograph (Micro GC Fusion, argon as the carrier gas, series number 70159886) was used to analyze the generation of H_2. During irradiation, the reaction system was stirred by a magnetic stirrer. Each reaction lasted 4 h, and all measured H_2 amounts were the average of three independent experiments. For comparison, hydrogen production was measured by dispersing 6 mg of P25 in 20 mL of an aqueous solution containing 25% TEOA.

Results and discussion

Characterization

XRD patterns of the produced materials are shown in Fig. 1. The crystalline structure of ZnO can be attributed to the wurtzite (ICSD 44477) structure.[29] It can be observed that the peak at 32°, corresponding to the plane (100), is more intense than the others. This result suggests a preferential growth in the (100) direction, which contradicts the literature. Typically, the direct growth of ZnO onto FTO films through similar routes, under conventional[30] or microwave conditions,[31] leads to preferential growth of the (002) plane (~34°). The XRD patterns of $BiNbO_4$ show a mixture of the orthorhombic and triclinic $BiNbO_4$. It is important to note that these two structures are expected to be formed under 1000 °C after 48–72 h;[15,32,33] when conventional heating sources are used during the synthesis. However, previous reports from our group using microwave-assisted synthesis have already led to the production of the phase mixture.[14,34] The color is strongly affected by the presence of the orthorhombic structure, as it is the phase that absorbs in the visible region. As discussed later, the $BiNbO_4$ reported here shows an intense yellow color,[15] possibly due to a high ratio of orthorhombic $BiNbO_4$. For the $BiNbO_4$/ZnO and $BiNbO_4/ZnO_T$ films, the observed XRD peaks are mainly ascribed to the ZnO wurtzite, including the preferential growth along the plane (100). The peaks ascribed to $BiNbO_4$ can be observed at the noise level and are shown in the insets of Fig. 1.

SEM images (Fig. S1†) show that the films are composed of vertically aligned ZnO nanorods with hexagonal shapes. The TEM images (Fig. 2a) show the nanorod morphology of ZnO, with an average diameter of 25.7 nm. The crystallinity of the ZnO materials was confirmed by the distinct lattice boundaries observed in the HRTEM images (Fig. 2b). The only identified lattice spacing of 2.46 Å corresponds to the (101) crystalline plane (ICSD 44477). The pattern diffraction obtained from the selected area electron diffraction (SAED) (Fig. S2†) confirms the polycrystallinity of the structure with concentric circles. Six crystalline planes of ZnO were identified, including (100), (101), (102), (103), (200), and (004). In addition, elemental mapping further supports the formation of ZnO, as evidenced by the distinct presence of zinc (Zn) and oxygen (O) elements (Fig. S3a†).

For the $BiNbO_4$, TEM images reveal particles with an elongated, rounded shape (Fig. 2c), exhibiting distinct sizes. The HRTEM image (Fig. 2d) confirmed the high crystallinity of the material, identifying a lattice spacing of 4.15 Å corresponding to the (1−11) plane of triclinic $BiNbO_4$, in agreement with the XRD results. No lattice fringes associated with orthorhombic $BiNbO_4$ were observed in the analyzed HRTEM images. Elemental mapping provides additional confirmation

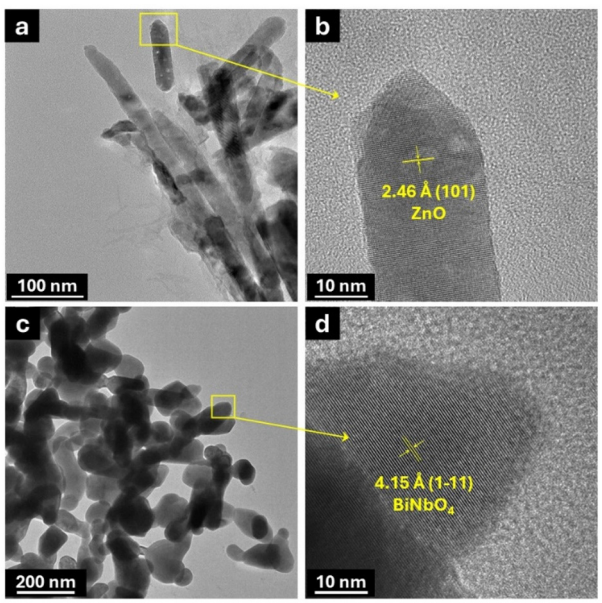

Fig. 2 TEM (a) and HRTEM (b) images of ZnO. TEM (c) and HRTEM (d) images of $BiNbO_4$.

‡Emission spectrum available at: https://www.heliosquartz.com/wp-content/uploads/2015/12/mercurio.jpg.

of $BiNbO_4$ formation, indicated by the unambiguous detection of bismuth (Bi), niobium (Nb), and oxygen (O) elements (Fig. S3b†).

TEM images of $BiNbO_4$/ZnO and $BiNbO_4$/ZnO_T films (Fig. 3a and e) reveal that the ZnO and $BiNbO_4$ particles are in close contact, exhibiting morphologies similar to those of pure materials. Diffraction patterns from the ZnO region display multiple diffraction rings, indicating a polycrystalline structure (Fig. 3b and f). The HRTEM images confirm the crystallinity of the materials through the clearly visible lattice boundaries (Fig. 3c and g). The ZnO particles exhibit a lattice spacing of 2.46 Å, corresponding to the (101) plane (ICSD 44477), consistent with the pure ZnO sample. $BiNbO_4$ particles show lattice spacing that corresponds to the (210), (121), and (040) planes of orthorhombic $BiNbO_4$. Elemental mapping confirms the presence of Zn, O, Bi, and Nb in both samples, verifying that the ZnO and $BiNbO_4$ particles are in close contact (Fig. 3d and h).

However, from the TEM images, it is impossible to understand the dispersion of the $BiNbO_4$ onto the ZnO or whether the heterojunctions have been formed. Therefore, KPFM was used to verify changes in the surface potential of the sample, which would be a consequence of the change in the work function (in this case, band gap). The KPFM results (Fig. 4) showed an increase in the heterogeneity of the surface potentials of the $BiNbO_4$/ZnO_T sample compared to $BiNbO_4$/ZnO, suggesting a change in the material's properties that may be attributed to band gap variations resulting from heterojunction formation. Both topography and KPFM images show a good alignment of ZnO and suggest a more homogeneous dispersion of $BiNbO_4$ onto the ZnO surface in the $BiNbO_4$/ZnO_T thin film.

XPS analysis was performed to confirm the chemical composition of the samples. The survey spectra (Fig. S4†) show the presence of bismuth, niobium, oxygen, and zinc (only on the spectra of the ZnO film and the heterojunctions). The O 1s XPS spectrum of ZnO film (Fig. 5a) shows a peak at the lower binding energy of 530.78 eV assigned to O^{2-} ions in the Zn–O bonding of the wurtzite structure of ZnO. High-resolution O 1s XPS spectrum of pristine $BiNbO_4$ (Fig. 5a) shows two peaks at 530.48 eV and 528.58 eV, corresponding to the O–Bi and O–Nb bonds, respectively.[35,36] The peak at 532.28 eV corresponds to the oxygen at the Nb–O bond of the Nb_2O_5 oxide form.[36] For the $BiNbO_4$/ZnO and $BiNbO_4$/ZnO_T samples, the O 1s XPS spectrum shows a peak at 530.58 eV that is slightly shifted in comparison to the peaks at similar binding energies found in the spectra of pristine $BiNbO_4$ and ZnO; also, the peak is broader. The observed peak probably corresponds to a combination of the O–Bi[35,36] bond and O^{2-} ions in the Zn–O bonding.[37] A second peak with lower intensity is observed at around 528.90 eV and can be ascribed to the O–Nb bonds.[35,36] The position of this peak is also shifted to a higher energy value when compared to the pristine $BiNbO_4$. These observations may suggest that oxygen is critical for the chemical bond between the species.

The high-resolution Nb 3d spectrum of pristine $BiNbO_4$ exhibits two peaks at 205.38 and 208.18 eV, corresponding to the Nb^{2+} 3d5/2 and Nb^{5+} 3d5/2 states, respectively (Fig. 5b). These features are associated with Nb atoms octahedrally co-

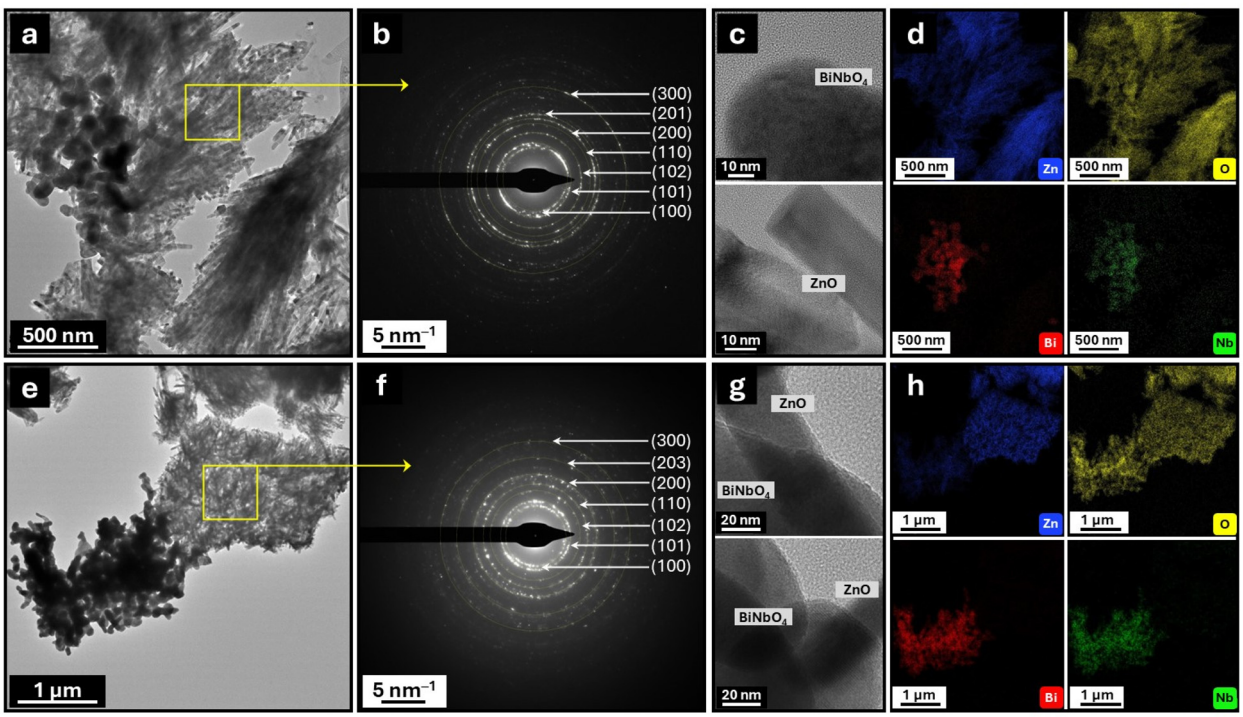

Fig. 3 TEM image (a), SAED (b), HRTEM (c) and elemental mapping (d) of $BiNbO_4$/ZnO film. TEM image (e), SAED (f), HRTEM (g) and elemental mapping (h) of $BiNbO_4$/ZnO_T film.

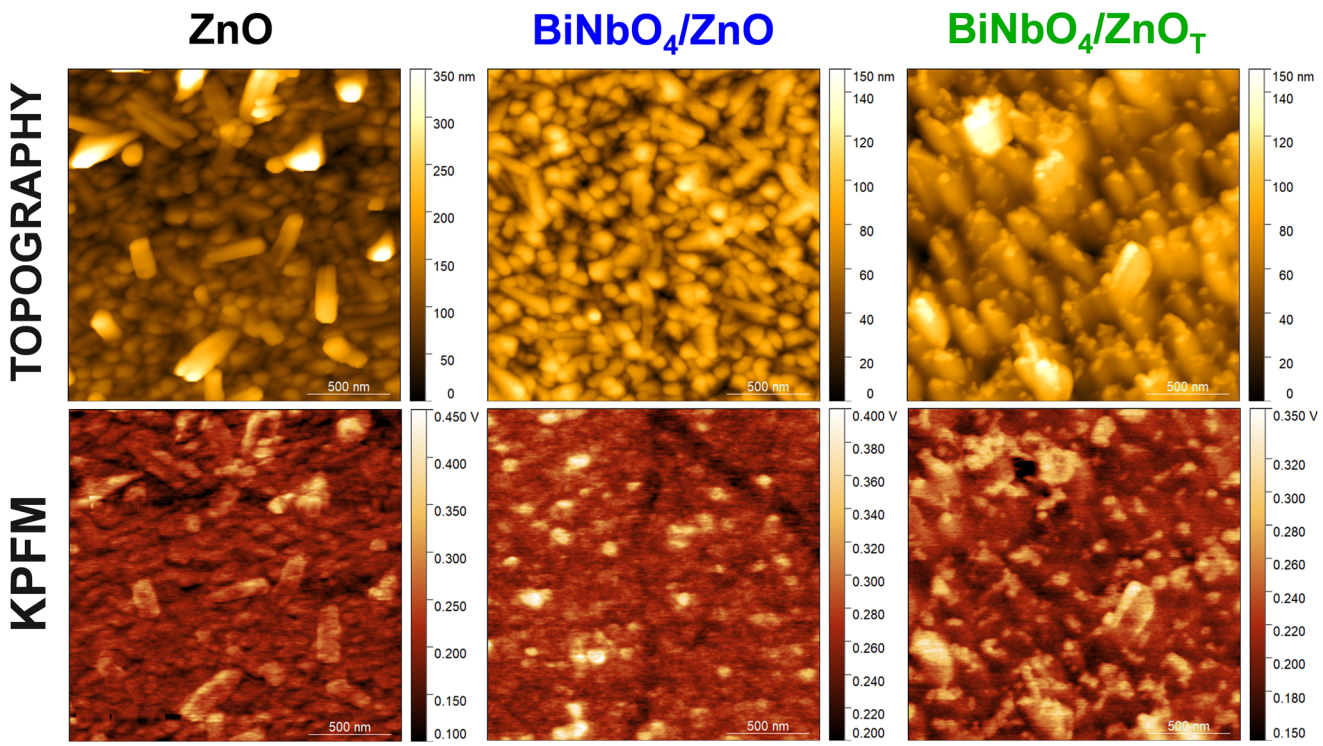

Fig. 4 Topography and KPFM images of ZnO $BiNbO_4$/ZnO and $BiNbO_4/ZnO_T$ samples.

ordinated to oxygen atoms, in which Nb atoms are surrounded by six oxygen atoms, resulting in distorted octahedra orthorhombic phase of Nb_2O_5 oxide.[35,36,38,39] While the Nb 3d spectrum of $BiNbO_4$/ZnO film does not show significant shifts, the spectrum of $BiNbO_4/ZnO_T$ film presents a slight shift to higher binding energy, indicating heterojunction formation.

The high-resolution Bi 4f spectrum of pristine $BiNbO_4$ exhibits two peaks at 157.78 and 163.08 eV, which can be ascribed to Bi $4f_{7/2}$ and Bi $4f_{5/2}$, respectively (Fig. 5c). They are related to the distorted trigonal bipyramidal of Bi_2O_3 oxide.[35,36,38–41] Again, no significant shifts in the binding energy were observed for the $BiNbO_4$/ZnO, film. In contrast, a slight shift to higher binding energy was observed for the $BiNbO_4/ZnO_T$ film, indicating heterojunction formation.

ZnO exhibits two distinct peaks at 1044.08 and 1021.08 eV, corresponding to the Zn 2p1/2 and Zn 2p3/2 core levels, respectively (Fig. 5d).[37] These results indicate that the chemical valence of Zn at the surface of ZnO corresponds to a +2 oxidation state.[37] The binding energy found on the Zn 2p high-resolution spectra of $BiNbO_4$/ZnO and $BiNbO_4/ZnO_T$ is shifted to lower energy, which can be ascribed to changes in the chemical environment. These complementary binding energy shifts, positive for Nb and Bi species and negative for Zn, establish a coherent charge transfer mechanism from the $BiNbO_4$ phase to the ZnO component, which is characteristic of successful heterojunction formation.[42] The magnitude and consistency of these shifts across the elements provide evidence for interfacial charge redistribution and the establishment of internal electric fields that facilitate enhanced charge separation in the composite photocatalytic system.[43]

The work function (φ) of ZnO and $BiNbO_4$ samples was determined from the secondary electron cutoff observed in the UPS spectrum using He–I excitation (Fig. 6a). The secondary electron onset on the left side of the spectrum was determined as 17.49 eV and 16.55 eV for ZnO and $BiNbO_4$, respectively. φ was then calculated as 3.73 eV and 4.67 eV for ZnO and $BiNbO_4$, respectively. The larger work function of $BiNbO_4$ in comparison to ZnO suggests that the band alignment in the $BiNbO_4$/ZnO and $BiNbO_4/ZnO_T$ forms a band bending at the interface, indicating the formation of an S-scheme structure.[44] The detailed calculation process is provided in the ESI.† The valence band maximum (VBM) was determined by linearly extrapolating the low binding energy edge of the valence band intersecting with the background in the XPS (Fig. 6b). The VB *vs.* NHE (pH 0) was calculated as 3.05 V and 3.92 V for ZnO and $BiNbO_4$, respectively. These values are expected for n-type semiconductors. The calculation process is also provided in the ESI.†

The UPS data were combined with the DRS results to assess the band structure of the heterojunction. The DRS spectrum of ZnO (Fig. 6d) shows an overlap in the visible and near-infrared regions. A similar behavior is observed for pristine $BiNbO_4$, which shows lower reflectance between 400–500 nm than ZnO. The band gap energies were estimated using the Kubelka Munk Function (detailed calculation is shown in the ESI†). By plotting the $[F(R) \times h\nu]^2$ *vs.* $h\nu$, the direct band gap values were

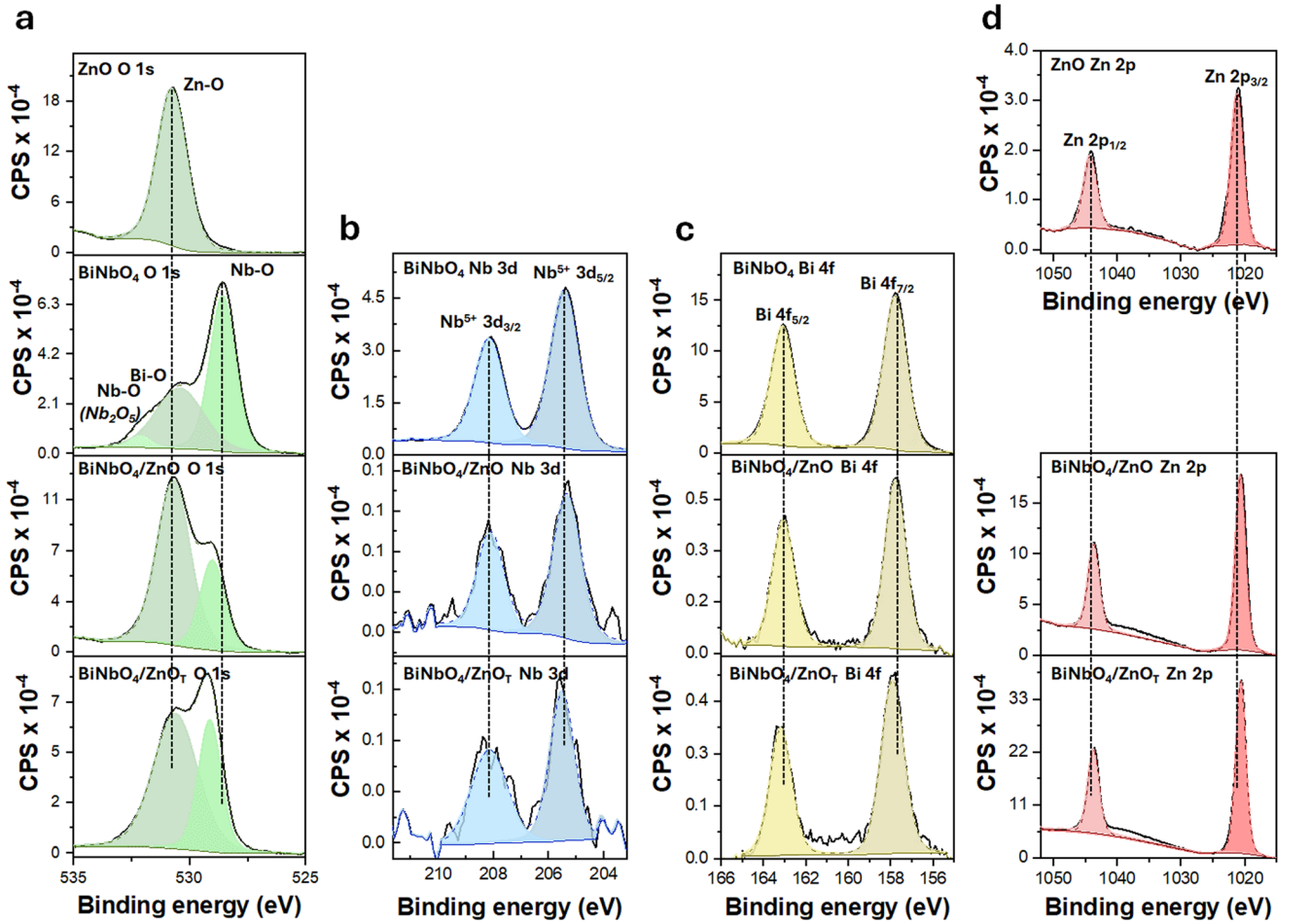

Fig. 5 High-resolution O 1s (a), Nb 3d (b), Bi 4f (c) and Zn 2p (d) XPS spectra of ZnO, $BiNbO_4$, $BiNbO_4$/ZnO and $BiNbO_4/ZnO_T$ films.

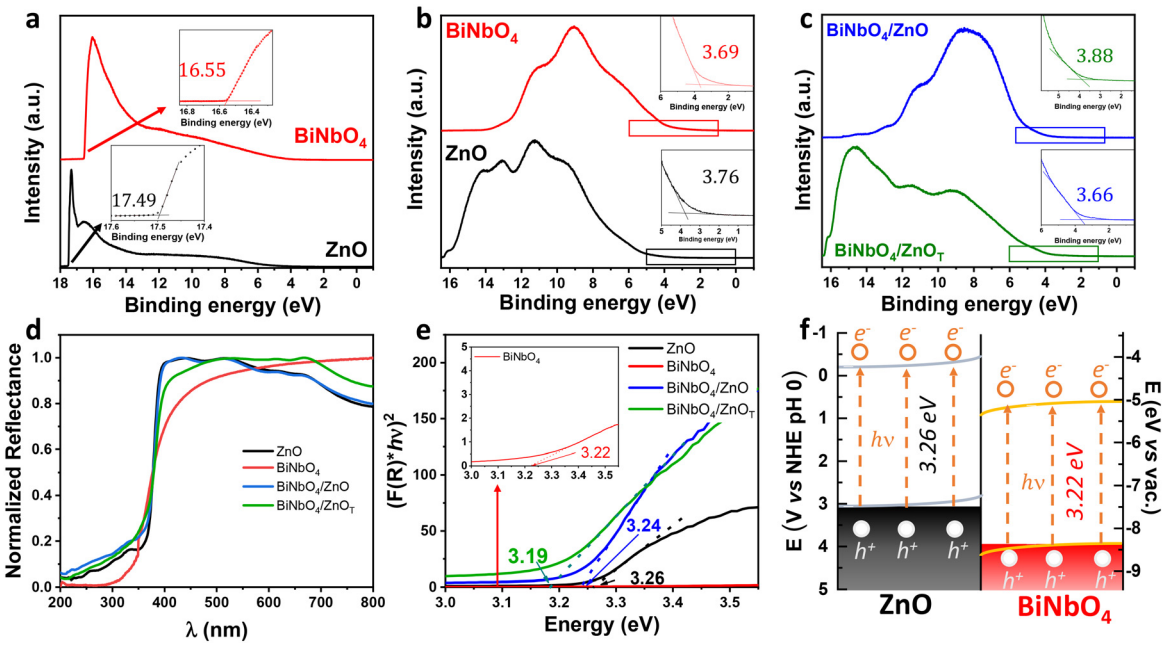

Fig. 6 Ultraviolet photoelectron spectra (He–I) of pure ZnO and $BiNbO_4$ (a). Valence band spectra (XPS) of pure ZnO and $BiNbO_4$ (b). Valence band spectra (XPS) of $BiNbO_4$/ZnO and $BiNbO_4/ZnO_T$ (c). Normalized reflectance spectra (d) and direct band gap energies (e) of ZnO, $BiNbO_4$, $BiNbO_4$/ZnO and $BiNbO_4/ZnO_T$ films. Schematic representation of the band structures for ZnO and $BiNbO_4$ after contact (e).

determined (Fig. 6e). The calculated band gap of ZnO is 3.26 eV, consistent with the literature.[19] For pristine $BiNbO_4$, the estimated band gap is 3.22 eV, which can be attributed to the contribution of the triclinic phase. Based on these values, the conduction band minimum (CBM) potentials *vs.* NHE (pH 0) were calculated as −0.21 V and 0.70 V for ZnO and $BiNbO_4$, respectively (see calculations in the ESI†). Fig. 6f shows the proposed band alignment of the heterojunctions, derived from the combined UPS and DRS data.

Moreover, as depicted in Fig. 6c, the VB spectra of $BiNbO_4$/ZnO and $BiNbO_4/ZnO_T$ indicate a shift in the VBM compared to both pristine $BiNbO_4$ and ZnO (Table S1†). These changes reinforce the hypothesis of a band banding due to the formation of heterojunctions.[45] The band gap energies of $BiNbO_4$/ZnO and $BiNbO_4/ZnO_T$, calculated from DRS (Fig. 6e), also suggest electronic transitions resulting from heterojunction formation, where the observed shift relative to the individual components is attributed to band bending. However, the DRS spectrum of $BiNbO_4/ZnO_T$ resembles that of pristine $BiNbO_4$. The band gaps of $BiNbO_4$/ZnO and $BiNbO_4/ZnO_T$ were calculated to be 3.24 eV and 3.19 eV, respectively. This change aligns with the results obtained from KPFM. Finally, combining the estimated band gap energies and VBM positions, the CBM values can be calculated as 0.49 V and 0.21 V *vs.* NHE pH 0 for $BiNbO_4$/ZnO and $BiNbO_4/ZnO_T$, respectively. These values lie between the CB potentials of the individual components, which indicates changes in the band potentials due to the combination of the materials through the method we reported here. Therefore, the collected evidence supports the hypothesis of heterojunction formation in $BiNbO_4$/ZnO and $BiNbO_4/ZnO_T$. However, the calcination process caused slight changes in the band gap and band edges of the resulting material, which may affect its applicability, as discussed later.

The dynamics of excess charge carriers in the photocatalysts and their recombination kinetics were investigated using TRMC measurements (Fig. 7a). In ZnO-based samples, electron mobility is significantly higher than hole mobility,[46] and thus, $\Delta\sigma(t)$ (eqn (1)) primarily reflects the behavior of the excess of electrons in the conduction band. A similar observation was also made for TiO_2 (P25), which has been analyzed for comparison purposes. The $BiNbO_4$/ZnO and $BiNbO_4/ZnO_T$ samples exhibit reduced I_{max} values compared to ZnO (53, 43, and 64 mV, respectively). This decrease can be attributed to the reduction of surface recombination centers,[27,28] likely resulting from the formation of the S-scheme structure. For the $BiNbO_4$ sample, no TRMC signal was obtained; in this case, no conclusion can be drawn for this material. Although further insight could be gained from analysing the decay kinetics, the signal was too noisy to allow for a reliable interpretation.

To better understand the role of the heterojunction in enhancing the photogenerated charge separation efficiency, steady-state photoluminescence (Fig. 7b) and TRF measurements were carried out for all samples (Fig. 7c). The PL spectra reveals that the emission intensities of both heterojunctions ($BiNbO_4$/ZnO > $BiNbO_4/ZnO_T$) are significantly lower than

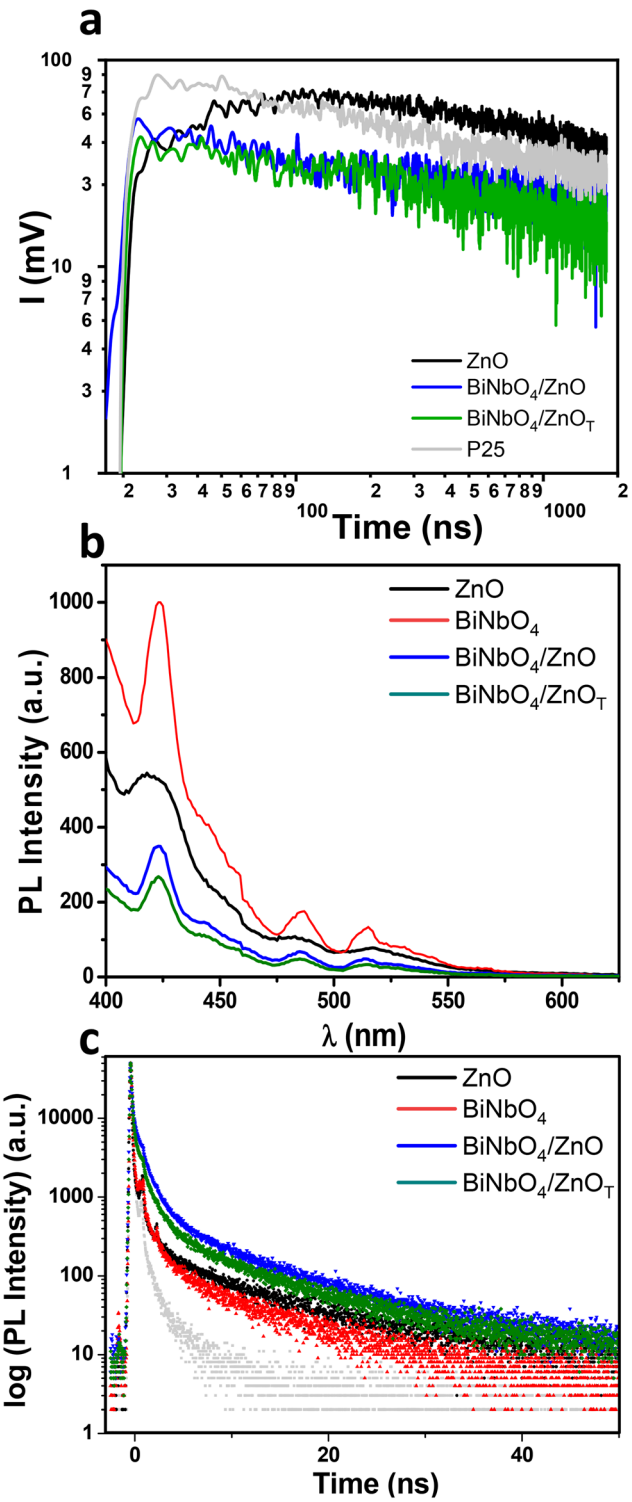

Fig. 7 TRMC signal of ZnO, $BiNbO_4$/ZnO, $BiNbO_4/ZnO_T$ films and P25 powder induced by 360 nm light pulses at 1 mJ cm^{-2} excitation density (a). PL spectra of ZnO, $BiNbO_4$, $BiNbO_4$/ZnO and $BiNbO_4/ZnO_T$, recorded with the excitation wavelength of 375 nm at room temperature (b). TRF spectra of spectra of ZnO, $BiNbO_4$, $BiNbO_4$/ZnO and $BiNbO_4/ZnO_T$, recorded with the excitation wavelength of 375 nm at room temperature and monitored at 424 nm (c), background is displayed in grey.

those of the individual oxide films ($BiNbO_4$ > ZnO). The deactivation process of the photogenerated electron in each film can explain this variation in the PL intensities.[47–49] In pristine ZnO and $BiNbO_4$, electrons are excited from the VB to the CB at a specific excitation wavelength. These electrons then recombine with the holes in the VB, resulting in a PL signal that reflects charge carrier recombination. In contrast, in the heterojunction samples, in addition to electron–hole recombination, and charge transfer between the oxides can also occur. This transfer process reduces the radiative recombination, as evidenced by the lower PL intensity. I particular, the reduced PL intensity observed for the $BiNbO_4/ZnO_T$ film suggests a lower rate of charge carrier recombination and a more efficient charge transfer process.

Moreover, the TRF results indicate that recombination occurs rapidly in ZnO and $BiNbO_4$ but is slowed down in the heterojunctions. It was impossible to distinguish the time decay between $BiNbO_4$/ZnO and $BiNbO_4/ZnO_T$ due to their similar PL lifetimes. However, the observed trend provides direct evidence that the photogenerated charge separation is enhanced upon heterojunction formation.[50–52] These results align with those from TRMC measurements, which also indicate efficient photogenerated charge separation in both heterojunctions.

Photoelectrochemical experiments

To determine the flat band potentials, Mott–Schottky plots were obtained using eqn (2):[53]

$$\frac{1}{C^2} = \left(\frac{2}{e\varepsilon\varepsilon_0 N_d}\right)\left[V_a - V_{fb} - \frac{kT}{e}\right] \quad (2)$$

where C is the space charge layers capacitance, e is the electron charge, ε is the dielectric constant, ε_0 is the permittivity of vacuum, N_d is the charge carrier density, V_a is the applied potential, and V_{fb} is the flat band potential. The flat band potential V_{fb} was determined by taking the x intercept of a linear fit to the Mott–Schottky plot, $1/C^2$, as a function of applied potential (V_a), Fig. 8a. All materials showed positive slopes, indicating n-type semiconductor behavior. The V_{fb} of ZnO film was determined to be −0.30 V, which is in accordance with previously reported data.[54] For pristine $BiNbO_4$, the V_{fb} was less negative (−0.69 V) than other structures of bismuth niobates.[55] In the $BiNbO_4$/ZnO sample, the V_{fb} was very similar to that of pure ZnO (−0.24 V), suggesting limited charge contact between the two components of the heterojunction. In contrast, the $BiNbO_4/ZnO_T$ heterostructure showed an intermediate V_{fb} value (−0.59 V), falling between the values found for the individual components. This result reinforces the hypothesis of a heterojunction formation. Measurements at additional frequencies (Fig. S6 and Table S2†) confirmed the consistency of the V_{fb} values obtained.

The N_D can be derived from eqn (2), resulting in eqn (3):

$$N_D = \frac{2}{\varepsilon\varepsilon_0 e}\frac{dE}{d\frac{1}{C^2}} = \frac{2}{\varepsilon\varepsilon_0 e}\frac{1}{\text{slope}} \quad (3)$$

where the slope refers to the linear portion of the Mott–Schottky plots. In other words, the plots in Fig. 8a can be used to extract the charge carrier density from their slope. It can be observed that pristine $BiNbO_4$ and $BiNbO_4/ZnO_T$, exhibit gentler slopes compared to ZnO and $BiNbO_4$/ZnO $BiNbO_4$, indicating a higher charge carrier density for the former two materials.

The photoactivity of each electrode was determined by measuring the current density during the oxygen evolution reaction (OER) under AM1.5G simulated solar light, irradiated on the front side of the film. Fig. 8b exhibits the chopped-light linear sweep voltammetry results. It can be observed that $BiNbO_4$/ZnO and $BiNbO_4/ZnO_T$ show higher photocurrents compared to pristine ZnO and $BiNbO_4$ films. For $BiNbO_4$ films, the current densities are significantly lower and indistinguishable in Fig. 8b; therefore, the corresponding linear voltammogram is presented in Fig. S7.† $BiNbO_4/ZnO_T$ generated higher photocurrents than $BiNbO_4$/ZnO. This result can be attributed to the synergistic effect of the heterojunction formed between $BiNbO_4$ and ZnO, combined with improved particle coalescence due to the post heat treatment applied to the $BiNbO_4/ZnO_T$ film, which increases the charge separation and, consequently, the lifetime of photogenerated charge carriers. These findings are consistent with the trends observed in the TRMC, PL, and TRF results (Fig. 7). Also, the lower energy band gap observed can facilitate the photogeneration of charges. For the $BiNbO_4$/ZnO, the results suggest the formation of a heterojunction with lower charge transfer capacity, which still improves the activity of the resultant material (in comparison to pristine $BiNbO_4$ and ZnO); however, it does not reach the same efficiency as the $BiNbO_4/ZnO_T$ film.

The photocurrents obtained for $BiNbO_4/ZnO_T$ heterojunction are slightly lower than those observed for $BiNbO_4/WO_3$ heterojunction.[13] However, it is important to note that the onset potential for $BiNbO_4/ZnO_T$ heterojunction is more negative than that of $BiNbO_4/WO_3$ heterojunction. In addition, the $BiNbO_4/ZnO_T$ heterojunction exhibits higher photocurrents at lower potentials and better stability at higher potentials. These results make the $BiNbO_4/ZnO_T$ heterojunction a more promising material than the previously reported $BiNbO_4/WO_3$ heterojunction.[13] While the photocurrent is lower than that reported by Arunachalam and coworkers (see ref. 12 and Table 1), it is worth noting that their study was conducted in a strongly basic medium, which can significantly influence performance. Chronoamperometry experiments (Fig. 8c) show that ZnO exhibits a fast charge injection upon light irradiation, followed by a fast decay, suggesting fast recombination of photogenerated charges. In contrast, $BiNbO_4$ shows inefficient charge injection, with a slow increase in current upon illumination that fails to reach a stable state and remains much lower than that of ZnO. The $BiNbO_4$/ZnO generates higher photocurrents than either ZnO or $BiNbO_4$. Its charge injection is faster than $BiNbO_4$ but slower than ZnO, and it does not show fast recombination. $BiNbO_4/ZnO_T$ exhibits similar behavior to $BiNbO_4$/ZnO, with a faster charge injection process and higher photocurrent. All photoanodes demonstrate good stability over time.

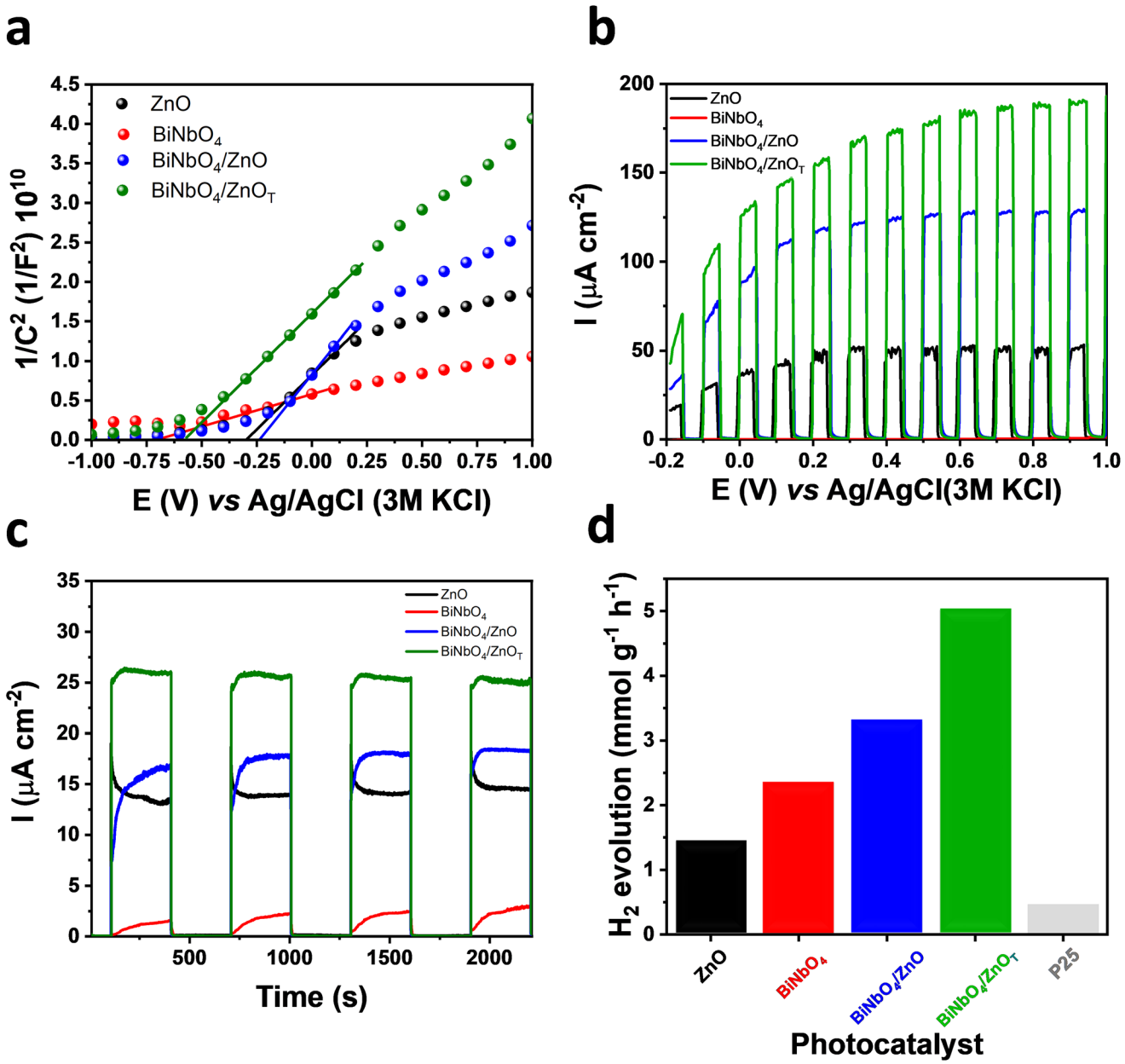

Fig. 8 Mott–Schottky plots at 1 kHz (a) chopped-light linear sweep voltammetry (b) and chopped-light chronoamperometry (c) of ZnO, $BiNbO_4$, $BiNbO_4$/ZnO and $BiNbO_4/ZnO_T$ films under simulated sunlight conditions. Hydrogen production from TEOA (25%) in water solution under UV irradiation measured by gas chromatography.

These results suggest that the synergistic effects of the heterojunctions lead to a material capable of producing a greater number of photogenerated charges due to the reduced recombination rates. These conclusions are consistent with the TRMC, PL and TRF data.

Hydrogen generation

Due to the high band gap potential of the heterojunction components, the photocatalytic activity of the films was investigated through hydrogen evolution reactions under UV light (Fig. 8d). To estimate the mass of photocatalyst used in each experiment, the materials (FTO coated with the photocatalyst) were washed, dried, and weighed. They were then immersed in a 10% (v/v) aqueous solution of aqua regia for 10 min to dissolve the ZnO deposition. The remaining FTO glass was washed, dried, and weighed again. The mass difference was assumed to correspond to the amount of catalyst used in each hydrogen evolution measurement. Due to the low sample masses, an ultra-microbalance was used for accurate measurement. Among the tested films, ZnO film produced the lowest amount of hydrogen, 1.43 mmol g^{-1} h^{-1}; however, this value is still higher than previously reported in the literature for

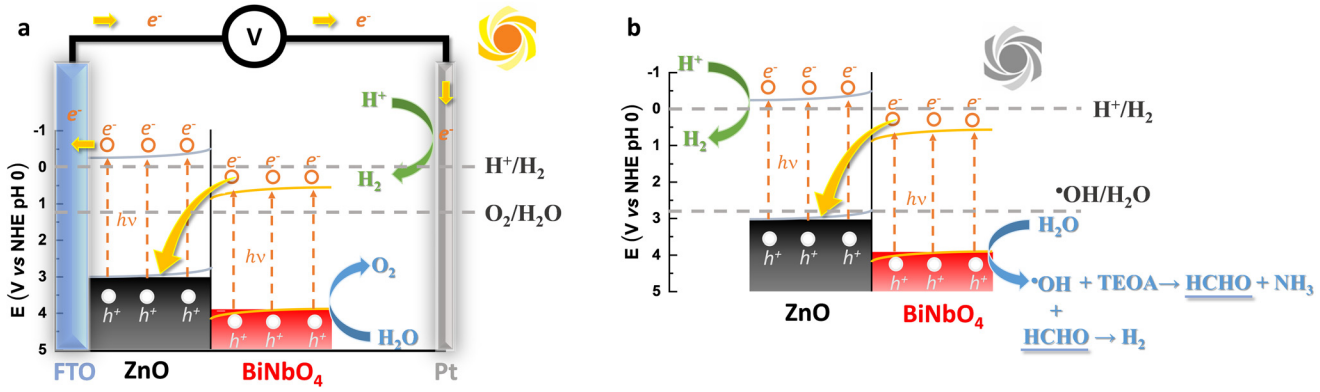

Fig. 9 Schematic representations of the possible reaction mechanism of photoelectrocatalytic water oxidation process (a) and photocatalytic H_2 production (b) over the S-scheme $BiNbO_4$/ZnO and $BiNbO_4$/ZnO_T heterojunctions.

ZnO.[56,57] Surprisingly, pristine $BiNbO_4$ produced 2.34 mmol g^{-1} h^{-1} of H_2, contradicting the trend observed in the photoelectrochemical measurements. This result can be ascribed to the use of a hole scavenger (TEOA) in photocatalytic measurements. Moreover, this result is significantly higher than the value reported by Dunkle and co-workers (Table 1),[2] who synthesized $BiNbO_4$ *via* a solid-state method. The $BiNbO_4$/ZnO and $BiNbO_4$/ZnO_T heterojunctions produced 3.28 and 5.01 mmol g^{-1} h^{-1} of H_2, respectively, indicating a significant enhancement in photocatalytic performance upon forming heterojunctions. The kinetics of H_2 production (Fig. S8†) show a continuous increase in H_2 generation over time, suggesting sustained activity. Notably, all synthesized materials outperformed commercial P25, which, despite showing a higher I_{max} in TRMC measurements, exhibited poorer performance, likely due to its higher charge recombination compared to ZnO, $BiNbO_4$/ZnO, and $BiNbO_4$/ZnO_T, as evidenced by the faster TRMC decay.

Mechanism

The combined evidence indicates that the $BiNbO_4$/ZnO and $BiNbO_4$/ZnO_T heterojunctions form an S-scheme structure. Under photoelectrochemical conditions (Fig. 9a), both oxides generate electrons and holes when simulated sunlight is applied. The photogenerated electrons are transferred from the CB of $BiNbO_4$ and recombine with the holes at the VB of ZnO. The remaining holes at the VB of $BiNbO_4$ oxidize water to O_2, while the photogenerated electrons at the CB of ZnO flow through the FTO to the external circuit up to the Pt counter electrode, where H^+ is reduced to H_2.

Regarding the photocatalytic generation of H_2 *via* TEOA photoreforming, the same S-scheme charge transfer process occurs (Fig. 9b). In this case, H_2 is produced both by H^+ reduction by the photogenerated electrons in the CB of ZnO and through the oxidation of TEOA. Notably, better hydrogen generation was observed under UV light irradiation.

The photocatalytic mechanism is likely, even though the estimated value for the conduction band of ZnO is less negative than −0.41 V. It is critical to highlight that the band structure was estimated based on the combination of the band edges determined for the individual components, which can be slightly different on the heterojunctions, as suggested in the UPS data. Thus, the dual path for photocatalytic H_2 production remains likely due to the lower recombination and higher electron lifetime observed for the heterojunction. The exact mechanisms have been proposed for similar heterojunctions using TEOA as a hole scavenger.[58,59]

Conclusions

Here, microwave irradiation produced vertically aligned ZnO nanorod films, which were then combined with $BiNbO_4$ to form two different heterojunctions. The first material was prepared without an annealing step ($BiNbO_4$/ZnO), while the second was submitted to thermal treatment ($BiNbO_4$/ZnO_T). The detailed characterization of the synthesized materials, including XRD, SEM and TEM, confirmed the successful mixture between the components. KPFM, XPS, UPS, and optical studies, as well as Mott–Schottky plots, indicated the formation of a heterojunction. Both heterojunctions exhibited an S-scheme structure, which enhances the separation of photogenerated charge carriers. This proposition aligns with the results of TRMC, TRF, and PL. Slight differences in the properties indicated that the thermal treatment enhanced the coalescence and stability of the $BiNbO_4$/ZnO_T, thereby fostering higher photo(electro)catalytic activity. The superior activity of $BiNbO_4$/ZnO_T in both oxygen evolution (under photoelectrochemical conditions) and hydrogen evolution (under photocatalytic conditions) confirms its potential as a highly efficient material. Therefore, this study demonstrates the successful synthesis of a bismuth niobate-based material with enhanced activity, making it a promising material for photocatalytic and photoelectrocatalytic applications, particularly hydrogen generation. This material has significant potential for future optimizations and technological applications, surpassing previously reported systems, such as pristine orthorhombic $BiNbO_4$ and the $BiNbO_4$/WO_3 heterojunction. This advance-

ment is especially relevant in the Brazilian context, where abundant niobium reserves present an opportunity to diversify the applications of this strategic metal.

Author contributions

M. K. contributed to methodology, investigation, formal analysis, validation, and visualization. P. H. P. contributed to the investigation, formal analysis, and visualization. C. H. C. contributed to the investigation. J. J. S. A. and C. C. J. contributed to investigation and formal analysis. H. R. contributed with validation and resources. J. S. S. contributed with conceptualization, supervision, resources, methodology, investigation, formal analysis, validation, data curation and visualization.

Conflicts of interest

There are no conflicts to declare.

Data availability

The data supporting this article have been included as part of the ESI.†

Acknowledgements

This work was supported by FAPESP (grants 2017/50332-0, 2021/05958-4 and 2023/12948-0). This study was also financed in part by the Coordenação de Aperfeiçoamento de Pessoal de Nível Superior – Brasil (CAPES) – Finance Code 001. The authors also acknowledge Conselho Nacional de Desenvolvimento Científico e Tecnológico (CNPq). M. K. acknowledges CAPES (grants 88882.451641/2019-01 and 001) and IPEN (grant 2020.06.IPEN.33PD2) for the doctoral and postdoctoral fellowships. J. S. S., P. H. P. and C. H. C. acknowledge the financial support from the Brazilian National Agency for Petroleum, Natural Gas, and Biofuels (grants 045919 and 2024/11637-4). Finally, the authors thank the Multi-users platform (CEM) at UFABC and the Institut de Chimie Physique – CNRS-Université Paris-Saclay for instrumental facilities.

The authors acknowledge Mireille Benoit for her help with the experiments in the ICP chemical laboratory.

References

1 L. Wang, W. Z. Wang, M. Shang, S. M. Sun, W. Z. Yin, J. Ren and J. Zhou, *J. Mater. Chem.*, 2010, **20**, 8405–8410.
2 S. S. Dunkle and K. S. Suslick, *J. Phys. Chem. C*, 2009, **113**, 10341–10345.
3 Z. H. Ai, W. K. Ho and S. Lee, *Appl. Surf. Sci.*, 2012, **263**, 266–272.
4 J. G. Hou, R. Cao, Z. Wang, S. Q. Jiao and H. M. Zhu, *J. Hazard. Mater.*, 2012, **217**, 177–186.
5 Y. M. Shen, Q. H. Wei, W. J. Guo, L. H. Fan, D. B. Liu and S. F. Li, *J. Alloys Compd.*, 2015, **618**, 311–317.
6 J. R. Fang, J. F. Ma, Y. Sun, Z. S. Liu and C. Gao, *Solid State Sci.*, 2011, **13**, 1649–1653.
7 H. N. Zhang, Y. K. Xiao, Z. Y. Shi, L. H. Tian, Y. L. Tang, X. M. Liu, Y. Y. Tian and Y. Lin, *J. Dispersion Sci. Technol.*, 2023, **45**, 80–90.
8 H. H. Gan, G. K. Zhang and Y. D. Guo, *J. Colloid Interface Sci.*, 2012, **386**, 373–380.
9 Y. L. Min, F. J. Zhang, W. Zhao, F. C. Zheng, Y. C. Chen and Y. G. Zhang, *Chem. Eng. J.*, 2012, **209**, 215–222.
10 S. Q. Zhang, Y. X. Yang, Y. N. Guo, W. Guo, M. Wang, Y. H. Guo and M. X. Huo, *J. Hazard. Mater.*, 2013, **261**, 235–245.
11 H. Jin, Y. Guo, J. Zhao, Y. Bei, Z. Wu and Q. Shang, *Sep. Purif. Technol.*, 2023, **311**, 123276.
12 M. Arunachalam, K. S. Ahn and S. H. Kang, *Phys. Chem. Chem. Phys.*, 2020, **22**, 14042–14051.
13 M. Kuznetsova, S. A. A. Oliveira, B. S. Rodrigues and J. S. Souza, *Top. Catal.*, 2021, **64**, 748–757.
14 S. A. A. Oliveira, M. Kuznetsova and J. S. Souza, *Ceram. Int.*, 2023, **49**, 10795–10806.
15 C.-Y. Lee, R. Macquart, Q. Zhou and B. J. Kennedy, *J. Solid State Chem.*, 2003, **174**, 310–318.
16 B. Muktha, J. Darriet, G. Madras and T. N. G. Row, *J. Solid State Chem.*, 2006, **179**, 3919–3925.
17 K. Yi, J. Zhang, W. Deng, Z. Mao, L. Tang and X. Chen, *IOP Conference Series: Earth and Environmental Science*, 2018, **170**, 032119.
18 H. Zhang, Y. Xiao, L. Tian, Y. Tang, X. Liu, Z. Shi, Z. Wu and Z. Wei, *Chem. Phys.*, 2022, **562**, 111644.
19 Z. Wang, H. Zhu, W. Tu, X. Zhu, Y. Yao, Y. Zhou and Z. Zou, *Adv. Sci.*, 2022, **9**, 2103744.
20 E. Samuel, B. Joshi, M.-W. Kim, M. T. Swihart and S. S. Yoon, *Nano Energy*, 2020, **72**, 104648.
21 S. Grushevskaya, I. Belyanskaya and O. Kozaderov, *Materials*, 2022, **15**, 4915.
22 J. Liu, Z. Luo, X. Mao, Y. Dong, L. Peng, D. Sun-Waterhouse, J. V. Kennedy and G. I. N. Waterhouse, *Small*, 2022, **18**, 2204553.
23 M. Tahir, S. Tasleem and B. Tahir, *Int. J. Hydrogen Energy*, 2020, **45**, 15985–16038.
24 V. Soni, P. Singh, A. A. P. Khan, A. Singh, A. K. Nadda, C. M. Hussain, Q. Van Le, S. Rizevsky, V. Nguyen and P. Raizada, *J. Nanostruct. Chem.*, 2023, **13**, 129–166.
25 H. Seok Jo, E. Samuel, H.-J. Kwon, B. Joshi, M.-W. Kim, T.-G. Kim, M. T. Swihart and S. S. Yoon, *Chem. Eng. J.*, 2019, **363**, 13–22.
26 B.-X. Zhou, S.-S. Ding, K.-X. Yang, J. Zhang, G.-F. Huang, A. Pan, W. Hu, K. Li and W.-Q. Huang, *Adv. Funct. Mater.*, 2021, **31**, 2009230.
27 A. L. Luna, E. Novoseltceva, E. Louarn, P. Beaunier, E. Kowalska, B. Ohtani, M. A. Valenzuela, H. Remita and C. Colbeau-Justin, *Appl. Catal., B*, 2016, **191**, 18–28.

28 A. A. Méndez-Medrano, D. Bahena-Uribe, D. Dragoe, C. Clavaguéra, C. Colbeau-Justin, J. P. Palomares Baez, J. L. Rodríguez-López and H. Remita, *Sol. RRL*, 2024, 2400106.
29 H. Schulz and K. H. Thiemann, *Solid State Commun.*, 1979, **32**, 783–785.
30 J. S. Souza, W. M. Carvalho, F. L. Souza, C. Ponce-de-Leon, D. V. Bavykin and W. A. Alves, *J. Mater. Chem. A*, 2016, **4**, 944–952.
31 D. Commandeur, G. Brown, E. Hills, J. Spencer and Q. Chen, *ACS Appl. Nano Mater.*, 2019, **2**, 1570–1578.
32 B. Muktha, J. Darriet, G. Madras and T. N. Guru Row, *J. Solid State Chem.*, 2006, **179**, 3919–3925.
33 O. Depablos-Rivera, A. Zeinert and S. E. Rodil, *Adv. Eng. Mater.*, 2018, **20**, 1800269.
34 M. Kuznetsova, S. A. A. Oliveira, B. S. Rodrigues and J. S. Souza, *Top. Catal.*, 2021, **64**, 748–757.
35 Z. Fang, L. Gao, H. Chen, K. Liang, Z. Liu, Z. Guan and J. Zhang, *Mater. Sci. Eng. B*, 2020, **259**, 114601.
36 N. Zhuk, V. Lutoev, B. Makeev, S. Nekipelov, A. Koroleva, A. Fedorova, M. Yermolina, D. Beznosikov and L. Karlova, *J. Mater. Res. Technol.*, 2020, **9**, 4173–4182.
37 R. Al-Gaashani, S. Radiman, A. R. Daud, N. Tabet and Y. Al-Douri, *Ceram. Int.*, 2013, **39**, 2283–2292.
38 K. Ławniczak-Jabłońska, I. N. Demchenko, E. Piskorska, A. Molak, J. Kachniarz and M. Heinonen, *Microchim. Acta*, 2004, **145**, 95–99.
39 I. Piir, D. Prikhodko, S. Ignatchenko and A. Schukariov, *Solid State Ionics*, 1997, **101**, 1141–1146.
40 C. Wang, H. Hu, S. Yan and Q. Zhang, *Chem. Phys.*, 2020, **533**, 110739.
41 S. Sood, S. K. Mehta, A. Sinha and S. K. Kansal, *Chem. Eng. J.*, 2016, **290**, 45–52.
42 P. S. Bagus, C. J. Nelin and C. R. Brundle, *J. Vac. Sci. Technol., A*, 2023, **41**, 068501.
43 Y. Li, L. Wang, F. Zhang, W. Zhang, G. Shao and P. Zhang, *Adv. Sci.*, 2023, **10**, 2205020.
44 B. Su, H. Huang, Z. Ding, M. B. Roeffaers, S. Wang and J. Long, *J. Mater. Sci. Technol.*, 2022, **124**, 164–170.
45 M. T. Uddin, Y. Nicolas, C. Olivier, W. Jaegermann, N. Rockstroh, H. Junge and T. Toupance, *Phys. Chem. Chem. Phys.*, 2017, **19**, 19279–19288.
46 J. Cui, *Mater. Charact.*, 2012, **64**, 43–52.
47 S. P. Adhikari, Z. D. Hood, K. L. More, I. Ivanov, L. Zhang, M. Gross and A. Lachgar, *RSC Adv.*, 2015, **5**, 54998–55005.
48 S. Adhikari and A. Lachgar, *J. Phys.: Conf. Ser.*, 2016, **758**, 012017.
49 V. Kumar, V. Kumar, S. Som, A. Yousif, N. Singh, O. Ntwaeaborwa, A. Kapoor and H. Swart, *J. Colloid Interface Sci.*, 2014, **428**, 8–15.
50 J. Zhang, X. Wang, X. Wang and C. Li, *Acc. Chem. Res.*, 2025, 1766–1769.
51 J. Ran, T. Y. Ma, G. Gao, X.-W. Du and S. Z. Qiao, *Energy Environ. Sci.*, 2015, **8**, 3708–3717.
52 B. Li, W. Peng, J. Zhang, J. C. Lian, T. Huang, N. Cheng, Z. Luo, W. Q. Huang, W. Hu and A. Pan, *Adv. Funct. Mater.*, 2021, **31**, 2100816.
53 F. Cardon and W. P. Gomes, *J. Phys. D: Appl. Phys.*, 1978, **11**, L63–L67.
54 F. Tezcan, A. Mahmood and G. Kardaş, *J. Mater. Sci.: Mater. Electron.*, 2018, **29**, 9547–9554.
55 M. F. Abou Taleb and M. M. Ibrahim, *Ceram. Int.*, 2024, **50**, 31985–31997.
56 Q. Li, P. Wu, Y. Huang, P. Chen, K. Wu, J. Wu, Y. Luo, L. Wang, S. Yang, Z. Liu and X. Guo, *Int. J. Hydrogen Energy*, 2022, **47**, 15641–15654.
57 W. Raza, K. Ahmad, R. A. Khan and H. Kim, *Int. J. Hydrogen Energy*, 2023, **48**, 29071–29081.
58 X. Guo, W. Ju, Z. Luo, B. Ruan, K. Wu and P. Li, *Int. J. Hydrogen Energy*, 2025, **98**, 1087–1098.
59 M. Xi, P. Wang, M. Zhang, L. Qin, S.-Z. Kang and X. Li, *Appl. Surf. Sci.*, 2020, **529**, 147200.